MLF Experimental Report	提出日 Date of report 2014 年 10 月 11 日
実験課題番号 Project No. 2013S01 実験課題名 Title of experiment 高分解能チョッパー分光器による物質のダイナミクスの研究 実験責任者名 Name of principal investigator 伊藤晋一、益田隆嗣* 所属 Affiliation 高エネルギー加速器研究機構、東京大学*	装置責任者 Name of responsible person 伊藤晋一 装置名 Name of Instrument/（BL No.） HRC (BL12) 利用期間 Dates of experiments 2013 年 4 月 － 2014 年 3 月

1．研究成果概要（試料の名称、組成、物理的・化学的性状を明記するとともに、実験方法、利用の結果得られた主なデータ、考察、結論、図表等を記述してください。

Outline of experimental results (experimental method and results should be reported including sample information such as composition, physical and/or chemical characteristics.

1. Introduction

The High Resolution Chopper Spectrometer (HRC) was installed and is being operated at BL12 in MLF, J-PARC, to study dynamics in condensed matters with high-resolutions and with relatively high-energy neutrons [1,2], under the framework of the S-type project. This project is aim to establish a comprehensive picture in condensed matter physics by observing wide range of correlated electron systems using the HRC. We selected some topics among them and focused on the following two points of view: high energy neutron studies on dynamical structures in metallic magnets, and, high accuracy studies on novel grounds states in low dimensional quantum spin systems.

We have optimized the performance of the HRC for this project. The HRC delivers high-resolutions and relatively high-energy neutrons for a wide range of studies on the dynamics of materials, and we proposed three types of experiments on the HRC, as indicated in Fig. 1. The first technique targets high-resolution experiments in a conventional energy momentum space (region A in Fig. 1). This experimental condition is useful for simultaneously determining a dispersion relation of excitations and details of the dynamical structure factor. The second technique aims to access the first Brillouin zone by using low-angle detectors and high-energy neutrons (region B). This is the so-called neutron Brillouin scattering (NBS). Observation of ferromagnetic spin waves from a polycrystalline sample becomes possible and should be useful for material development. The third technique opens the possibility of accessing eV region (region C). Dispersive excitations up to a sub-eV energy region can be observed by using single-crystal samples. Electronic excitations are expected to be observable, if eV neutrons are practically utilized.

In this report, we describe the construction, and the instrumental improvements after that, also the scientific results from this initial operation in the period between JFY2008 and JFY2013. Among these activities, in particular, the NBS method has been successfully launched, and demonstrations and results have been obtained. It should be noted that the HRC was constructed and is being operated under the collaboration between the Institute for Solid State Physics, the University of Tokyo and the Institute of Materials Structure Science, High Energy Accelerator Research Organization (KEK).

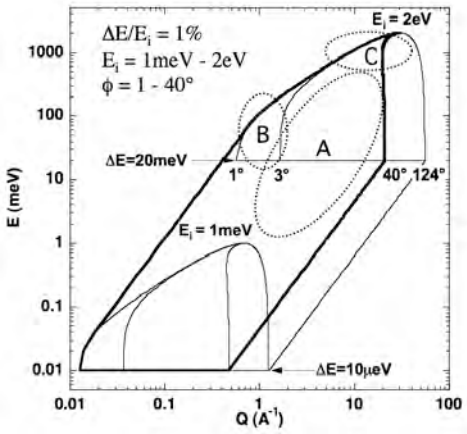

Fig. 1 Energy-momentum space for three techniques of high-resolution experiments A, B, C proposed for the HRC.

2. Design and Initial Construction

On a chopper spectrometer, a neutron beam is monochromatized by a Fermi chopper and then incident on a sample to be investigated. The neutrons scattered from the sample are detected by a neutron detector placed at a certain scattering angle. The energy transfer (E) and momentum transfer (Q) from the neutron to the sample are determined by measuring the time-of-flight (TOF) and the scattering angle (ϕ) of the detected neutron. The Fermi chopper consists of a slit package inserted to a cylinder rotating in synchronization with the production timing of pulsed neutrons. Neutrons pass through the slit package when it rotates to a position of the slit parallel to the incident neutron beam, and the slit-open time (chopper-open time) determines the energy resolution of the spectrometer. High energy neutrons from the pulsed neutron source are scattered and moderated within the spectrometer, resulting in a large amount of background noise. A T0 chopper reduces this noise by blocking the incident neutron beamline at around time zero. Also, to increase the neutron flux, a supermirror guide tube is mounted in the primary flight path.

A schematic layout of the HRC is illustrated in Fig. 2. The size parameters are L_1 = 15 m (the distance between the neutron source and the sample), L_2 = 4 m (the distance between the sample and the detector), and L_3 = 1 m (the distance between the Fermi chopper and the sample). The HRC at BL12 faces the decoupled moderator, which has an area of 100 mm × 100 mm, and the maximum sample size is assumed to be 50 mm × 50 mm. In this geometrical condition, the energy resolution is estimated to be $\Delta E/E_i$ = 2.5% (E_i: incident neutron energy) for the optimum condition where the chopper-open time Δt_{ch} is equal to the pulse width Δt_m, and the incident beam divergence is estimated to be $\Delta\phi$ = 5 mrad. The energy resolution can be improved when $\Delta t_{ch} < \Delta t_m$, with a concomitant reduction in the peak neutron intensity. For $\Delta E/E_i$ = 1%, the peak neutron intensity is 75% of that for the optimum condition, which we consider to be an acceptable tradeoff.

A supermirror guide tube was partially installed in the primary flight path at the shutter section (m = 3) and at the biological shielding section (m = 3.65), where m is the ratio of the critical wave number for the supermirror to that for natural nickel. However, the collimator tube without mirrors was installed instead of the guide tube (m = 4) in the down stream section due to the limited budget. The m values were determined by the financial budgets provided. The energy dependence of the flux gain of the guide tube was calculated by McStas, a large gain is expected for the full installation, as shown in Fig. 3.

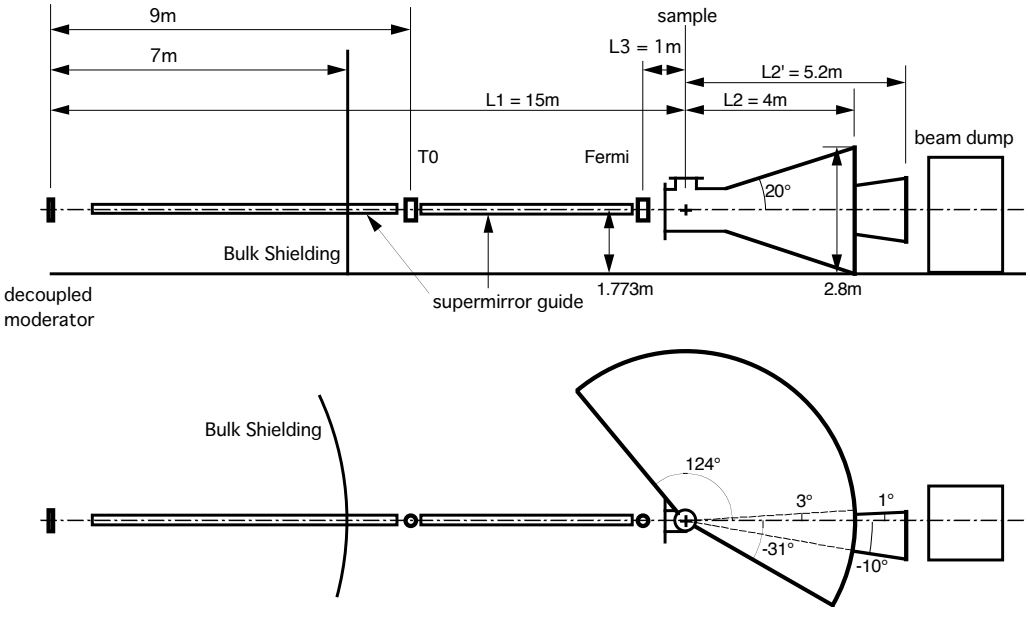

Fig. 2 Schematic layout of HRC.

必要に応じて、A4 サイズの用紙に続きを記入して下さい。

Please use A4-size papers for further reporting, if necessary.

A T0 chopper [3,4] was installed 9 m from the neutron source. At this position, the beam cross section is 76 mm × 76 mm. The size of the T0 chopper blade is 78 mm × 78 mm, which includes a ±1 mm margin for the beam cross section. The length of the blade along the beamline is 300 mm, and the blade is made of Inconel X 750, which was chosen for its mechanical strength and radiation properties. When the blade center is initially centered on the beamline, it takes 408 μs for the blade to be removed from the beam cross section, and this occurs at a 100 Hz rotational frequency and for a 300 mm rotational radius. The rotational axis is parallel to and under the beamline. Under these conditions, the HRC accepts neutrons with energy less than 2.5 eV. The margin of ±1 mm corresponds to a phase-control accuracy of ±5 μs at 100 Hz. We developed a phase control system which reduces the fluctuations in the rotational period down to 1 μs (FWHM: full width at half maximum) at 100 Hz at an off beam environment. Also, the fluctuations during beam time were measured to be approximately 3 μs (FWHM) at any rotational frequency. The observed fluctuations meet the requirement demanded by the phase-control accuracy within ±5 μs.

A newly developed Fermi chopper [5] was installed at L_3 = 1 m. We tried to develop the Fermi chopper by modifying a turbo molecular pump (TMP) with a magnetic bearing system. First, the TMP blade was replaced by the slit package, and we could rotate up to 600 Hz by the TMP controller. Next, we tried to design the phase control system of the Fermi chopper synchronized with the production timing of pulsed neutrons. We could drive the motor of this system by an external power supply and just by using the TMP controller as a magnetic bearing controller. Finally, we successfully developed the phase control system. Based on the developments, we produced the first model of the Fermi chopper made in Japan. The commercially available composites made of boron fibers were used for the slit materials. In this actual system, we confirmed the phase control accuracy less than 0.1 μs (FWHM) at 600 Hz against the timing of the external trigger at an off beam environment. A shifting mechanism of two Fermi choppers was also developed in order to select one of the choppers or white beam condition.

We mounted 2.8 m (effective length) PSDs (position sensitive detectors) inside the vacuum scattering chamber. Although it was possible to install detectors at $\phi = -31° - 124°$, the detectors cover at present only $\phi = -10° - 42°$ because of the recent limitations in He3 gas supplies. Therefore, the installed detector area is only 30% of the entire area. In the main detector area at $\phi = 3° - 42°$, 128 PSDs (effective length: 2.8 m, diameter: 0.75 inch, He3 gas pressure: 1.8 MPa) were mounted inside the vacuum scattering chamber for conventional experiments. At low angles ($\phi = -10° - 1°$), 123 shorter PSDs (0.8 m, 0.5 inch, 2 MPa; 0.6 m, 0.5 inch, 2 MPa; 0.6 m, 1 inch, 1 MPa; used at KENS or newly acquired) were mounted; some at L_2 = 4 m and the rest at L_2 = 5.2 m at the lowest angles. 20 pieces of the newly acquired PSDs (0.8 m, 0.5 inch, 2 MPa) located at around $\phi = \pm 0.5°$ inside the vacuum scattering chamber are used for the NBS experiments.

The PSDs used at KENS were mounted outside the vacuum scattering chamber, facing a thin Al window, of which area is about 1 m^2 and thickness is 1.5 mm, on the surface of the vacuum scattering chamber [6]. This size of the window should be designed in consideration of material properties up to the plastic region. B_4C liners were mounted on all the walls inside the vacuum scattering chamber to avoid spurious scattering. The compositions of particle size of B_4C was determined for minimizing water absorption into B_4C [7].

The data acquisition (DAQ) system for the HRC is illustrated in Fig. 4 [2]. Signals generated at a PSD are amplified by preamplifiers and sent to a readout module called NEUNET. When a neutron is captured at a PSD numbered n_{det}, the charges generated at both ends of the PSD are digitized and converted to pulse heights Q_1 and Q_2 by an analog-to-digital converter (ACD) in the NEUNET where, in an ideal case, the position u of the detected neutron within the PSD is given by $u = L_D Q_2/(Q_1+Q_2)$ with the PSD length L_D. A timing signal from the accelerator defining $t = 0$ is delivered by a GATENET to NEUNETs and the TOF of the detected neutron t is defined. The timing signal is gated by the device status, which is the phasing status of the choppers, the temperature control status of the sample, etc. Thus, the GATENET forwards the timing signal to the NEUNETs, only when the device status indicates that all the devices are operational. For detection of a neutron, the set $\{n_{det}, Q_1, Q_2, t\}$ is generated as an event datum (8 bytes/event) on the NEUNET. Event data can be accessed through a computer network with SiTCP. In addition, event data from the monitor detectors can be accessed at the GATENET through the computer network with SiTCP. One NEUNET, which uses the VME standard, controls 8 PSDs. A 19-inch VME rack can contain up to 20 NEUNETs for 160 PSDs. On the HRC, 251 PDSs are controlled by 33 NEUNETs, and a GATENET is also mounted on the VME rack. The event data are transferred by the computer network from the NEUNETs to the central processing unit (CPU). We prepared a CPU (POWER MASTER Server A8452 from System Works Co.) for the DAQ system (DAQ CPU), and installed Scientific Linux 5.4 as well as the DAQ middleware. Via the DAQ-Middleware, the DAQ-Operator configures the DAQ system and controls

DAQ-Components that control processes in the DAQ system. User commands such as begin/end of the data acquisition can be sent to the DAQ system through a web-browser user interface.

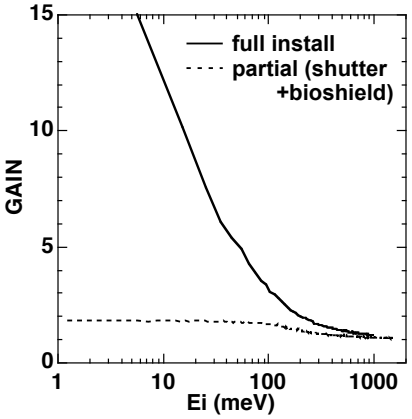

Fig. 3 Calculated flux gain of the guide tube on the HRC. In the measurements in Figs. 5 (a) - (c), the guide tube was partially installed (dashed line).

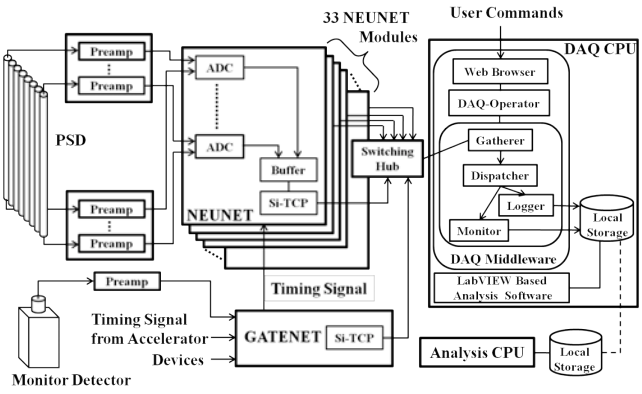

Fig. 4 DAQ system installed on the HRC.

3. Performance

To evaluate the HRC performance, a vanadium standard sample was mounted at the sample position on the HRC [1]. A monochromatic neutron beam with the Fermi chopper or a white neutron beam without the Fermi chopper was incident on the sample, and the scattered neutrons were detected with the array of 128 PSDs located at $\phi = 3° - 42°$. A monitor detector was located at 13.4 m from the neutron source (just upstream of the Fermi chopper). The neutron intensities detected by the monitor and that detected by the PSD array for the white beam are plotted in Figs. 5(a) and 5(b). The observed intensities were in good agreement with the calculations in the absolute values within a factor. Figure 5(c) shows the elastic scattering energy spectrum from the vanadium standard sample and detected by the PSD array for the incident neutron energy of E_i = 203 meV, with the optimum chopper (which provides roughly $\Delta t_{ch} = \Delta t_m$) at 600 Hz, as a function of the energy transfer. We chose E_i = 203 meV because the neutron transmission through the optimum chopper shows a maximum at 200 meV. The solid line is a calculated spectrum without any adjustable parameters. The energy resolution from the observed energy width was ΔE = 5.2 meV, and therefore $\Delta E/E_i$ = 2.5%. At E_i = 203 meV, the absolute magnitude of the neutron intensity for a monochromatic beam agreed with the calculation, and also it was confirmed that $\Delta E/E_i$ = 2.5% in the energy resolution as designed for the optimum condition. Assuming the optimum condition ($\Delta E/E_i$ = 2.5% with $\Delta t_{ch} = \Delta t_m$) for any E_i, the neutron flux for inelastic neutron scattering (INS) experiments at the sample position with a 1 MW proton beam for full installation of the guide tube is estimated as shown in Fig. 5(d).

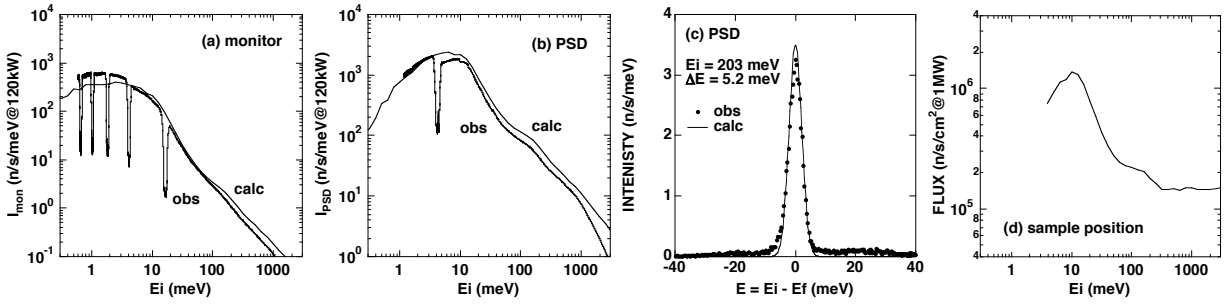

Fig. 5 Neutron intensities at the monitor (a) and at the PSD array (b) for white neutron beam. The dips in the observed data are caused by the operation of the T0 chopper. (c) Elastic-scattering energy spectrum at PSD array for vanadium standard sample with E_i = 203 meV. (d) Expected neutron flux at sample position for the optimum condition $\Delta E/E_i$ = 2.5% for 1 MW proton beam.

The T0 chopper is a key device to reduce the background noise that originates from high-energy neutrons emitted during neutron production. Figure 6 (a) shows the TOF spectrum observed at the PSD array from the standard vanadium sample with the T0 chopper running at the rotational frequency of 100 Hz, and with the

T0 chopper off and the blade removed from the beamline [1]. The sloppy chopper was used as the Fermi chopper and operated at 600 Hz. Since the slit width of the sloppy chopper is coarse, the neutron beam passes through the sloppy chopper every half turn, then many peaks appear. The neutron energy of the peak at TOF = 2000 ms corresponds to 0.5 eV. We successfully reduced the background noise at neutron energies near 0.5 eV by two orders of magnitude. This indicates that INS experiments that require the detection of very small signals can be conducted on the HRC. Figure 6 (b) shows the T0 chopper transmission as a function of TOF measured using the standard vanadium sample and detected at the PSD array with the white neutron beam. We confirm that the transmission recovers below 2.5 eV of the neutron energy at 100 Hz, as designed. The energy for 50% transmission at 100 Hz is 10 eV, and then neutrons with energies up to several eV can be used with only a slight reduction in neutron intensities.

Therefore, we confirmed that the observed neutron intensities and the resolutions of the HRC in the initial construction well agreed with the designed performance [1].

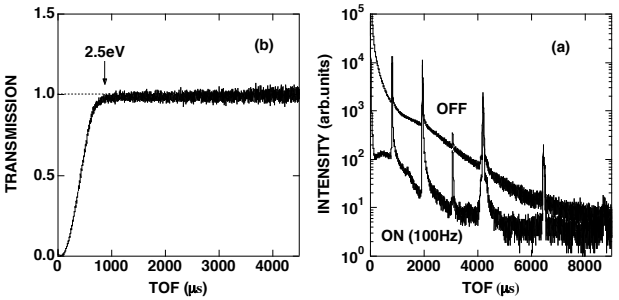

Fig. 6 (a) Background noise reduction for monochromatic neutron beam. The TOF spectra with operating the T0 chopper at 100 Hz (ON) and without operation (OFF) are indicated. (b) TOF dependence of the transmission at 100 Hz measured with the white neutron beam.

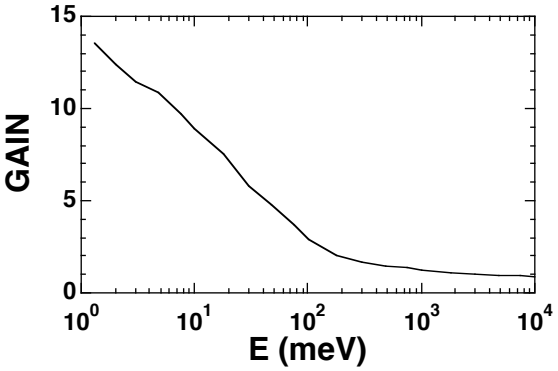

Fig. 7 Observed gain of the supermirror guide system on HRC, which is the ratio of the intensity of scattered neutrons from a vanadium sample detected at the PSD array from 3° to 42° in the present set-up including the newly installed guide tube to that in the previous set-up.

4. Improvement in instrumentation

Since the above initial construction, we have continuously improved the HRC at many points as described below. In particular, by the installation of the collimator system as well as the full guide tube, the NBS experiments have been feasible on HRC.

On the primary flight path of L_1 = 15 m, the supermirror guide tube was initially installed in the shutter and the biological-shielding sections of 4.6 m. After that, the collimator tube in the down stream section was replaced by a supermirror guide tube of 5.2 m [8]. By the present installation, we obtained a great intensity gain by a factor of 3 at E_i = 100 meV and a factor of 5 at E_i = 50 meV in comparison with the previous set-up, as shown in Fig. 7.

A Soller collimator system composed of slits of vertical sheets of Cd with a thickness of 0.1 mm was installed just upstream of the sample, and the collimation can be chosen to be 2.3° and 0.6° automatically [8]. Since there was a huge background noise at low angles, as shown in Fig. 8 (upper), a measurement with an empty can was required. Figure 8 shows excitation spectra in a one-dimensional (1D) antiferromanget, $CsVCl_3$, measured at T = 20 K. By using the 2.3° collimator, the background at low angles was greatly reduced and a spectrum from the sample can be obtained without an empty scan, as shown in Fig. 8 (lower). In the lower angle region, PSDs are installed down to 0.5°. These low angle detectors as well as sub-eV incident neutrons enable the NBS experiments on the HRC [9]. Figure 9 shows observed spectra from an empty can at ϕ = 0.64° with E_i = 102 meV. A spread of the direct beam at E = 0 meV and a spurious peak at E = 5 meV were observed with the collimator with the 0.6° collimation. The direct beam spread was eliminated and the spurious peak was reduced by using the collimator with the 0.3° collimation. The spurious peak at E = 5 meV, originating from a reflection of the direct beam at a position near the PSDs, could be successfully eliminated by masking the position with a cadmium plate. Finally, based on these developments, 2.3° and 0.3° collimators were replaced by 1.5° and 0.2° collimators, respectively.

An experimental control environment was developed to combine the measurements of neutron counts with the control of devices such as choppers, temperature controllers, goniometers, vacuum system, and so on, as shown in Fig. 10 [8]. The HRC Control Platform was developed and installed on the computer named DAQ-OP (DAQ operator). The HRC Device Control Software controls the devices as well as the DAQ middleware (DAQ MW) via the Control LAN through the Platform. The HRC Experiment Control Software

executes a sequence composing begin/end of measurements and controls of devices. At present, almost all the devices on the HRC can be controlled through this platform and these operations can be connected with the data acquisition (begin/end of measurements). In order to optimize the computing environment, the composition of the computers was improved.

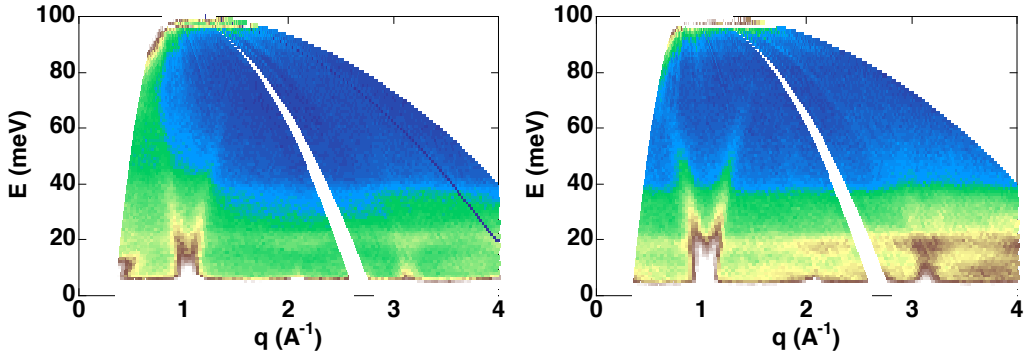

Fig. 8 Excitation spectrum from $CsVCl_3$ measured with E_i = 102 meV on HRC, for the previous set-up (upper) and the present set-up with the 2.3° collimator and the full guide tube (lower). The intensities (color) are normalized by the number of protons incident to the neutron production target. The noise at low-q has been greatly reduced by the collimator, also the neutron flux has been increased by the full guide tube.

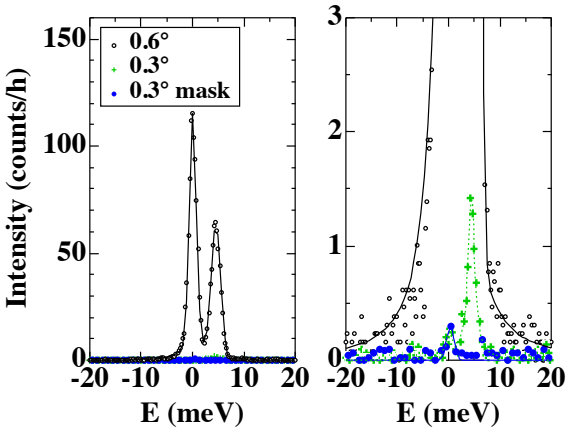

Fig. 9 Background noise at ϕ = 0.64° for the 0.6°, the 0.3° collimators, and the 0.3° collimator with a cadmium mask at the position of the direct beam hit. The incident neutron energy was selected to E_i = 102 meV, The same data are plotted in both figures with different scales for the vertical axes. The lines are guides to the eye.

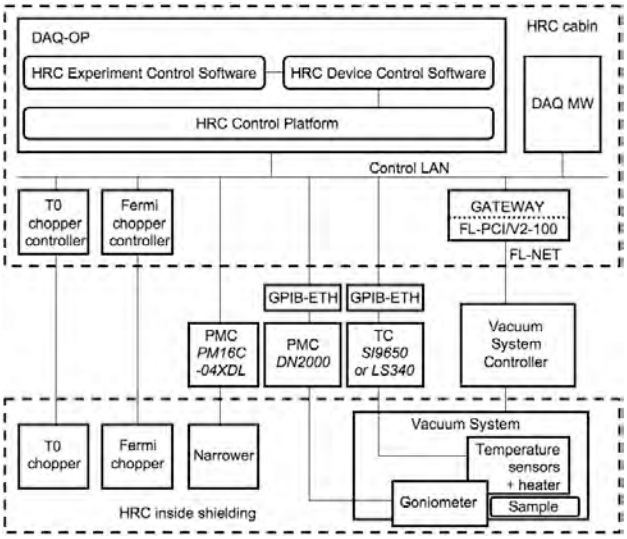

Fig. 10 Experimental control environment on the HRC. PMC, TC, GPIB-ETH represent a pulse motor controller, a temperature controller, a GPIB/Ethernet converter, respectively. The vacuum system is accessible through the Gateway server and the FL-net. The incident neutron beam is controlled by the Fermi chopper and the narrower, and the sample environment such as the temperature and the crystal angle is controlled. The operation status of the T0 chopper and the vacuum system is monitored.

We also developed the software to analyze single crystal sample data as well as powder sample data. The analyzed data can be transformed to the standard Mslice format for a convenience of users. Also, the process for the alignment of the sample crystal became very easy. The excitation spectra in the three-dimensional system on the four-dimensional energy-momentum space can be also measured by rotating the crystal axis of the sample, and visualized.

Initially, we installed two Fermi chopper: one is a so-called sloppy chopper for high intensities and the other is optimized for E_i = 200 meV at 600 Hz with the optimum condition. And therefore, the optimum condition was realized in the energy range of E_i = 10 – 200 meV. At present, we installed a Fermi chopper optimized for E_i = 500 meV at 600 Hz, and then the energy range for the optimum resolution of $\Delta E/E_i$ = 2.5 – 3 % was extended up to E_i = 500 meV [8].

In the initial construction, the sample area was separated from the vacuum scattering area near PSDs with a thin Al foil in the vacuum scattering chamber, and the sample area was evacuated by a small TMP to achieve a high vacuum around the sample area. The TMP was replaced by a cryopump with a pumping speed

of 28 m^3/s and the Al foil was removed. A gate valve with a diameter of 750 mm was also mounted between the cryopump and the chamber. A cryopump system is now used for evacuating the vacuum scattering chamber encompassing the sample and the flight path of the scattered neutrons. After installing this system, the regeneration process of the cryopump, which is the process to release absorbed molecules, was optimized and a frequency of the evacuation without the regeneration was greatly reduced.

For conventional INS experiments, 128 pieces of 2.8m PSDs, which are mounted into two detector banks, covers $\phi = 3 - 42°$ at present. PSDs for another two detector banks were purchased, and they will be installed soon.

64 pieces of 2.8m PSDs are mounted on each detector bank panel of 1.5 m × 3 m with a vacuum flange, and two panels with PSDs are hold on the vacuum scattering chamber. To remove the panel from the vacuum chamber, it was necessary to remove the shielding block above the vacuum scattering chamber first, and then, remove the panel by using a crane installed at the experimental hall. At present, we mounted a rail on the vacuum chamber body just above each panel, and the panel can be removed from the chamber along the rail by using a hand chain hoist. By using this mechanism, we replaced the damaged PSDs by new ones in a much easier procedure without removing the shielding.

Since the cadmium slits were successful for the incident beam collimator, an oscillating radial collimator was manufactured for the collimation of the scattered neutron beam.

The deck connecting the space of BL12 to the mezzanine was constructed. Therefore, the mezzanine in the 1st experimental hall of MLF was completed. Close to the deck, a chopper maintenance area was constructed.

In order to cool the sample down to 4 K stably, a GM-type refrigerator was installed. This refrigerator shows a good cooling performance by improving the radiation shielding.

A cryomagnet to apply the magnetic field up to 14 T to the sample was designed, manufactured and delivered. We started the commissioning at the Guide Hall of JRR-3M, and confirmed that it was successfully operated with the maximum magnetic field of 14 T.

Due to the earthquake disaster on 11 March 2011, some pieces of 2.8m PSDs were damaged and some shieldings were slipped on the HRC. We realigned the beamline, restored the shieldings, replaced the damaged PSDs with new ones, and confirmed the operations of the choppers, the vacuum system, and the electronics. After these recovery works, the neutron production target at the MLF received the proton beam in December 2011 and the neutron scattering experiments were started in January 2012.

The vacuum scattering chamber and its vacuum system were installed in 2009. The maintenance for them was performed in September 2012. The property of the large thin Al window on the surface of the chamber was also confirmed to be normal.

During the partial mounting of the new PSDs, a vacuum leakage occurred in March 2014. To find the leakage point, all the thin Al windows were removed and replaced by thick plates, because of the safety regulation. The low angle detectors mounted outside the vacuum were removed. Fortunately, the leakage points were at the vacuum connections of PSDs, not at the Al windows. At present, although the high vacuum is recovered, the low angle detectors mounted outside the vacuum are still removed. However, the PSDs for the NBS experiments are mounted in the vacuum.

5. Neutron Brillouin Scattering Experiments

5.1 Feasibility of NBS on HRC

On the HRC, the NBS experiments became feasible by reducing the background noise at low scattering angles down to $\phi = 0.5°$. NBS is the most promising way to observe excitations in the forward direction from powders, polycrystals, or liquids. Owing to the kinematical constraints of neutron spectroscopy, incident neutron energy (E_i) in the sub-eV region is necessary for measuring scattering in the meV transferred energy (E) range close to (000), and with a high energy resolution of $\Delta E/E_i$, further, the scattered neutrons need to be detected at very low scattering angles (ϕ). Low angle detectors are essential to access the present energy momentum space. In fact, the region above the dashed line in Fig. 11, which is the envelope of scan loci for $\phi = 5°$ with respect to E_i, can never be accessed using a conventional spectrometer with the lowest scattering angle of $\phi = 5°$, for instance.First, NBS experiment was performed on the HRC to observe spin waves in a polycrystalline sample of a cubic perovskite, $La_{0.8}Sr_{0.2}MnO_3$, (Curie temperature: T_C = 316 K). Magnetic properties of this material are well elucidated and it has been already reported that spin waves were measured by using a single crystal sample. Figure 11 shows the dispersion relation of spin waves in $La_{0.8}Sr_{0.2}MnO_3$ measured with E_i = 100 meV, where DE/E_i = 2%. The observed dispersion relations at 6 and 245 K were

well fitted to $E = DQ^2$, where Q is the scattering vector. The D values were obtained to be 130 ± 13 and 88 ± 2 meVÅ^2 at 6 and 245 K, respectively. These values are in good agreement with the results (D = 131 and 89 meVÅ^2 at 14 and 250K, respectively) obtained by the previous INS experiments using a single crystal. Therefore, the feasibility of NBS experiments on the HRC was demonstrated [9-11].

5.2 Spin dynamics in metallic ferromagnet $SrRuO_3$

Spin waves in a polycrystalline ferromagnet $SrRuO_3$ (T_C ~ 160 K) were measured, because a large single crystal suitable for INS experiments has not yet been synthesized. The measurement was performed at 7 K with E_i = 100 meV, and well-defined spin wave peaks were observed. As shown in Fig. 11, the dispersion relation of spin waves in $SrRuO_3$ was well fitted to $E(Q) = E_g + DQ^2$ with an apparent energy gap E_g [10]. Also, the temperature (T) dependence of D and E_g was investigated. We found that $D(T)$ was almost independent of T up to T_C, and $E_g(T)$ could be related to the anomalous Hall conductivity. These results might syggest the intermediate electron correlation in $SrRuO_3$ as well as the vital role of magnetic monopoles in momentum-space as a source of strong Berry curvature originating from the spin-orbit interaction [12].

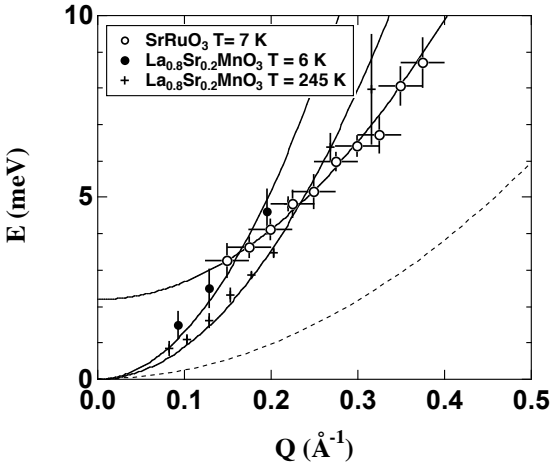

Fig.11 Spin-wave dispersion curves for $La_{0.8}Sr_{0.2}MnO_3$ and $SrRuO_3$ determined on the HRC. The solid lines are fitted curves. The dashed line is the upper boundary accessible with a conventional spectrometer with the lowest angle of ϕ = 5°.

5.3 Spin waves in permanent magnet $Nd_2Fe_{14}{}^{11}B$

$Nd_2Fe_{14}B$ is a well-known song permanent magnet with T_C = 580 K and the saturation magnetization of 1.6 T. At room temperature, all spins are aligned along the c*-axis. Below 130 K the system exhibits a spin reorientation. Because the unit cell includes four chemical formulae of $Nd_2Fe_{14}B$ in a tetragonal lattice, spin-wave branches are expected to be complicated. In a previous INS experiment using a single-crystalline sample of $Nd_2Fe_{14}{}^{11}B$, a spin-wave branch was detected only along the c*-axis around (002) at 6 and 295 K [13]. We performed NBS experiments in a $Nd_2Fe_{14}{}^{11}B$ polycrystalline sample at 6 and 300 K with E_i = 257 meV and ΔE = 5.7 meV [11,14]. The observed spin-wave peaks at 300 K were well fitted to Gaussian scattering functions with widths determined from the resolution, and the peak positions were determined in Fig. 13. The observed peak positions were on the dispersion curve along the c*-axis reported in the previous experiment using a single crystal [13]. No magnetic peaks were observed at 6 K, this result is also consistent with the reported dispersion at 6 K.

5.4 Phononic excitations in liquid D_2O

Phononic excitations in a liquid D_2O were measured at 300 K with E_i = 102 meV and ΔE = 2.0 meV [11]. The observed spectra showed excitation peaks and a resolution-limited elastic peak. The excitation peaks were fitted with a damped harmonic oscillator scattering function convoluted with the instrumental resolution width multiplied by a temperature factor and the peak positions $E(Q)$ were determined. The present analysis was identical to that for the previous inelastic neutron scattering experiment [15]. As shown in Fig. 14, the Q dependence of the observed peak positions down to Q = 0.02 Å^{-1} was well fitted to E(Q) = cQ with c = 21.4 ± 0.2 meVÅ, which is equivalent to c = 3250 ± 30 m/s. The observed sound velocity c was

in good agreement with that for the fast sound observed in the previous experiment with E_i = 80 meV and ΔE = 4.8 meV down to Q = 0.035 Å^{-1} [15].

5.5 Collective dynamics of hydrated β-lactoglobulin

Protein hydration plays a fundamental role in protein behavior: water-protein interactions affect protein folding, maintain structural integrity, mediate molecular recognition, and accelerate enzymatic catalysis. Many scattering measurements, both elastic and inelastic, and many molecular dynamics simulations, have been performed to investigate the relation between protein dynamics and that of the surrounding solvent molecules. Single particle dynamics of proteins and hydrated water have been investigated using incoherent scattering from hydrogen in hydrated protein powder. On the other hand, the investigation of collective dynamics of proteins and hydrated water using coherent scattering is relatively scarce, although it contains important information of structure and dynamics. First, we performed NBS experiment of pure D_2O at room temperature on the HRC, as mentioned above. The fast sound mode due to the collective dynamics of water was detected as well as the inelastic X-ray scattering [16]. Next, hydrated β-lactoglobulin powder was measured at 180 – 298 K. The sample dimension was 40 x 40 x 8 mm^3. Figure 15 shows INS signals of the sample at different Q values. The spectra show well-defined acoustic excitations as shoulders (see arrows in the figure) that change in excitation energy with Q in the low Q region. The dispersion relation observed in inelastic X-ray scattering measurement [17] was found in the present study. The high-frequency sound velocity obtained from the dispersion relation was almost independent of T and 2460 ± 110 m s^{-1} at 298 K.

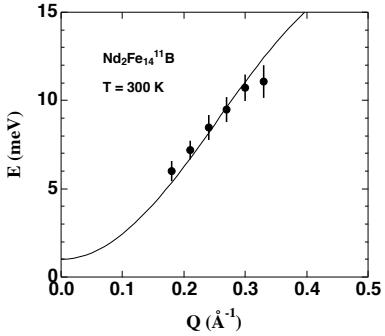

Fig. 13 Spin wave dispersion relation of $Nd_2Fe_{14}{}^{11}B$. The solid line is the dispersion curve along the c^*-axis determined using a single crystal sample [13].

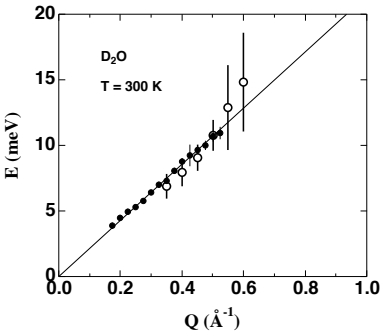

Fig. 14 Dispersion relation for phononic excitations, the fast sound, in D_2O (closed circles). The open circles are previous results in ref. [15]. The solid line is a fitted line.

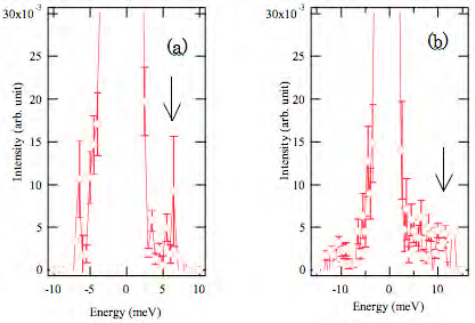

Fig. 15 Inelastic neutron spectra of hydrated β-lactoglobulin at 180 K at (a) Q = 0.25 Å^{-1} and (b) Q = 0.55 Å^{-1}.

6. Experiments in Conventional QE Space

6.1 Quantum renormalization effects in 1DHAFs

The ground state of a 1D Heisenberg antiferromagnet (HAF) with S = 1/2, where S is the spin quantum number of magnetic ions, is the degenerate singlet spin state (Bethe state). The lowest spin excitations from the Bethe state are renormalized from the classical spin-wave state excited from the Néel state. The excitation energy can be described by $E(q) = 4SRJ\,|\sin q|$ with the exchange constant J, and the enhancement is defined by the quantum renormalization factor R; R = p/2 for S = 1/2. On the other hand, it is well known that a system with S = 5/2 behaves classically (R=1). Figure 8 shows excitation spectrum for $CsVCl_3$ measured on the HRC, where spin excitations were well observed in the entire Brillouin zone up to the zone boundary energy and $E(q)$ could be determined as peak positions of spin excitations. To detect the S-dependent quantum renormalization effect, INS experiments were performed at KENS and ISIS using 1DHAFs: $CsNiCl_3$ (S = 1), $CsVCl_3$ (S = 3/2), $CsVBr_3$ (S = 3/2), and $CsCrCl_3$ (S = 2). At present, we improved the data for $CsVCl_3$ on the HRC, also newly analyzed data for the other materials [18]. W e measured the dynamical structure factor of spin excitations $S(q,E)$ to determine $E(q)$, as shown in Fig. 16. To determine the value of R, the J value should be obtained. The static spin correlation function $S(q)$ was

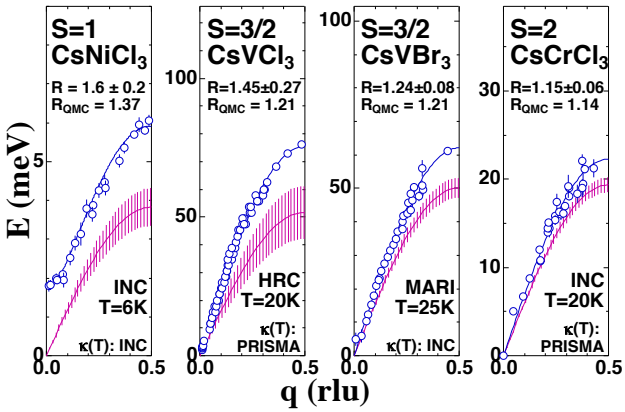

Fig.16 Dispersion relations of the lowest spin excitations in 1DHAFs. The solid lines on the data points (marks) are fitted dispersion curves. The sine curves with bars are those for classical spin waves estimated from J determined by κ(T).

deduced by integrating $S(q,E)$ over E, and the inverse correlation length k was obtained as the width of $S(q)$. The J value can be determined from $\kappa(T)$, which is described as a function of J for any S by a quantum theory. In Fig. 16, the classical dispersion relations estimated by J from $\kappa(T)$ are also shown with the uncertainties from the determination of J. The values of R, which is the ratio of $E(q)$ at the zone boundary (q = 0.5 rlu) to the classical spin wave energy, were in good agreement with those predicted by quantum Monte Carlo calculations.

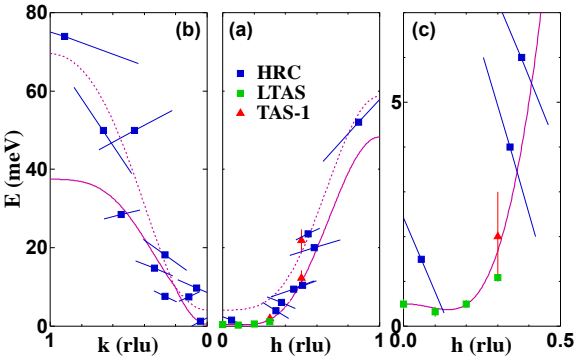

Fig. 17 Dispersion relation of spin waves in the ferromagnetic phase of MnP along the a^* (a) and b^* axes (b), with calculated curves for acoustic (solid line) and optical (dashed line) modes. The bars on the marks represent statistical errors along the scan directions. Low energy part along the a^* axis is indicated in (c).

6.2 Spin waves in ferromagnetic phase of MnP

MnP is ferromagnetic below 293 K, and transforms into a helical spin phase at 46 K. In the ferromagnetic phase, the easy axis of the magnetization is the c^* axis and the hardest one is the a^* axis. In the helical spin phase, the spin rotates in the b^*-c^* plane with a propagation vector of $0.117a^*$. Early INS studies suggested that the helical spin phase is caused by a delicate balance between exchange interactions [19], also reported that the spin wave dispersion relation in the ferromagnetic phase can not be described by the conventional q^2 law along the a^* axis [20].

We determined the spin wave dispersion relations in the ferromagnetic phase at 60 K, by using HRC as well as LTAS and TAS-1 at JRR-3M [21,22]. The Mn lattice in MnP deviates from a primitive orthorhombic lattice with displacement parameters u and v along the a and b axes, respectively, and therefore, the unit cell includes four Mn sites. Since v is negligibly small, the Mn lattice can be approximately divided into two sub-lattices. We consider an isotropic Heisenberg interaction adding a single ion anisotropy for two sub-lattices, and take into account of exchange interactions between Mn pairs up to the 6th neighbors. The observed peak positions of spin waves were well described by this model, as shown in Fig.17.

By using the HRC, spin waves were observed in a wide energy momentum space near to the zone boundary. In the calculation, the acoustic and optical modes are separated from each other along the a^* axis. Along the b^* axis, these two modes resonate with each other at around k = 0.2 rlu (reciprocal lattice unit) and switch roles, but the two modes are not crossed. Observed spin wave peak positions are well explained by the two modes. In fact, two spin wave peaks were clearly observed at h = 0.5 rlu on the TAS-1. As shown in Fig. 17 (c), the low energy part in the a^* axis for the presently-improved dispersion relation obtained by the LTAS was also well fitted to the present model, where the calculated dispersion curve along the a^* axis shows a minimum at around h = 0.14 rlu. This complicated q dependence is caused by the displacement parameter u, in fact, the minimum disappeared for u = 0.

We successfully observed spin waves in the ferromagnetic phase of MnP along the a^* and b^* axes in the entire Brillouin zone up to the zone boundary. The dispersion relations were well described by an isotropic Heisenberg model adding a single ion anisotropy with two sub-lattices, and the anomalous dispersion relation along the a^*-axis was found to be caused by the atomic displacement from the primitive lattice. The previous studies suggested that the anomalous dispersion is caused by an exchange competition [19] or itinerant nature of d electrons [20]. A recent structural study suggested the existence of the Dzyaloshinsky-Moria interaction [23]. To resolve these problems, further investigations are required.

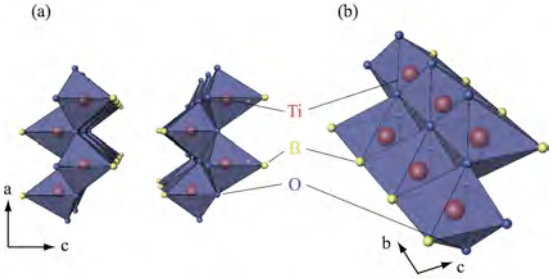

Fig. 18 Crystal structure of TiOBr. Ti ions (red) are surrounded by boron (yellow) and oxygen (blue) ions, forming quasi two-dimensional plane.

6.3 Mind the "Gap" on quantum spin systems

Quantum spins in a low-dimensional system show unusual quantum phases such as Haldane gap and spin-Peierls state, by the strong quantum nature. The spin singlet is the basic starting point for describing a ground state of the quantum spin chain. Another interest in a quantum spin systems is the cooperation among physical degrees of freedoms. The strong correlations between quantum spin and charge, orbital, and lattice are expected to give rise to a fascinating new quantum phase as a realization of high-T_c

superconductivity in two-dimensional (2D) system. Here, we report some of research results carried out by using the HRC.

1) Finding the gap in TiOBr: Newly proposed spin-Peierls system TiO*X* (*X*: Cl, Br) has been revealed showing 1D nature associated with orbital ordering of Ti ions and super-lattice structure being related to the Peierls instability. It is pointed out that resulting only from an arrangement of Ti d_{xy} orbital, the formation of 1D spin chains and the spin-Peierls transition will be realized. Recently, it has been demonstrated that TiOBr also exhibits two successive phase transitions, similar to TiOCl at $T_{c1} = 27$ K and $T_{c2} = 47$ K. INS experiments were carried out in order to find the direct evidence of spin-Peierls transition, namely, the spin gap. The inelastic spectrum with a large amount of poly- crystalline sample of TiOBr is expected to show the localized signal in the vicinity of the magnetic zone center $Q = 0.9$ Å^{-1}. This low-Q access measurement of polycrystalline sample is only achieved by a small angle (ϕ) and a high incident energy (E_i) condition. The detectors at around $\phi = 3°$ and $E_i = 200$ meV are used for searching the excitation at low-Q region. However, obtained $S(Q,E)$ shows no indication of the existence of magnetic signals in the spectrum except for phonon contribution. The gap energy in TiOBr is expected much higher from that measured thermodynamic properties and by analogy with TiOCl, and could be 20 meV in energy. It still remains as open questions if the spin-Peierls state under the cooperation of orbital ordering is realized in this system. The absence of the spin gap implies the ground state of TiOBr is *not* spin singlet state, but is possibly different state as spin liquid state.

2) Hole dynamics in a 1D spin chain: It is practically hard to realize the carrier doping in 1D material because the localization of carriers occurs at low T. We tested spin and hole dynamical properties in $Nd_{2-x}Ca_xBaNiO_5$, which is successfully hole doped 1D Haldane system. The lightly doped $x = 0.035$ carrier content were measured by means of pulsed neutron inelastic scatterin as shown in Fig. 19 [24]. It is clearly observed the entire one-magnon band with spin gap (Haldane gap) at magnetic zone center (MZC) addition to intense cystal field excitation of Nd ions. The zone boundary energy reaches 60 meV that is less comparing to undoped Haldane chain. On the other hand, the gap slightly increases in its energy, but still gap opens even holes doped (spin correlation of Haldane state is known to be spatially exponential). Moreover, new dynamical structures within the Haldane gap were observed upon carrier doping, showing incommensurate structures centered at MZC. This is originated by the dynamics of doped-holes. For further experiments, hole carrier dependence of Ni chain band (Haldane band) and hole dynamics will be focused

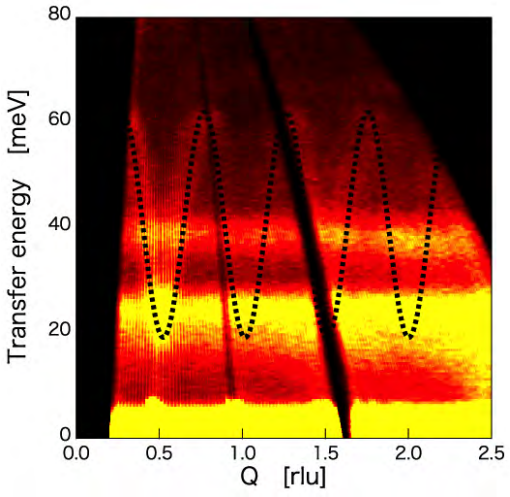

Fig. 19 S(Q,E) observed in $Nd_{1.965}Ca_{0.035}BaNiO_5$.

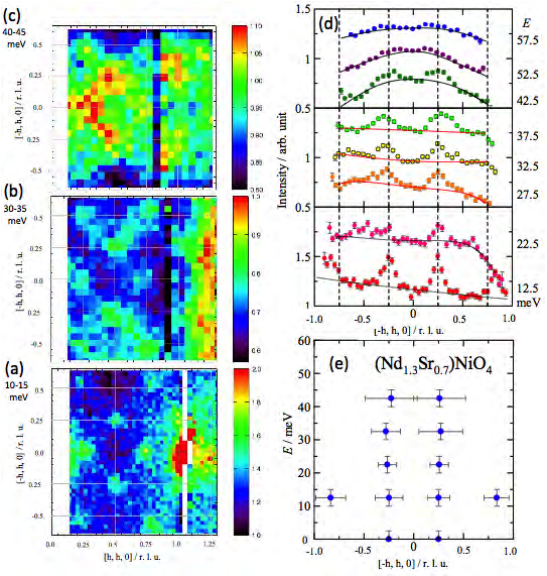

Fig. 20 INS measurements from $(Nd_{1.30}Sr_{0.70})NiO_4$ measured on the HRC. (a) - (c) Constant energy slices showing the variation of the intensity in the (h, k) plane at selected energies. The data are averaged over the range of energies indicated in the figure. (d) Constant energy cuts along the [-H, H, 0] directions at various energies. The data are averaged over (H, H) = (1.0, 1.0) ± (0.1, 0.1). (e) Dispersion of the magnetic excitations in $(Nd_{1.30}Sr_{0.70})NiO_4$ along [-H, H, 0] direction.

6.4 Unusual spin dynamics in the checkerboard order in 2D layered nickelate

When the antiferromagnetic insulating phase is melted by carrier doping in the layered transition-metal oxides, the hole doping stabilizes the non- trivial spin-charge ordering towards the metal- insulator transition. In particular, the doped carriers tend to form the stripe or simple square-lattice checkerboard patterns. Although the magnetic excitations in the insulating stripe phase can be described by the linear spin-wave approximation with in-plane anisotropic exchange parameters, a breakdown of the linear spin wave approximation was observed in the magnetic excitations in the checkerboard phase with higher carrier concentration. The spin dynamics in the checkerboard phase of $(La_{2-x}Sr_x)NiO_4$ ($x = 0.5$) and more metallic $(Nd_{2-x}Sr_x)NiO_4$ ($x = 0.6, 0.7$) are systematically investigated by INS experiments using a large single crystals grown by the floating-zone method. We found that the observed magnetic excitations in the checker- board phase is qualitatively different from those of the more insulating stripe phase. They do not show behavior of

counter-propagating spin wave branches up to $E \sim 70$ meV as shown in Fig. 20, but are rather similar to those in the high T_c cuprates which show straight-up chimney-like excitations.

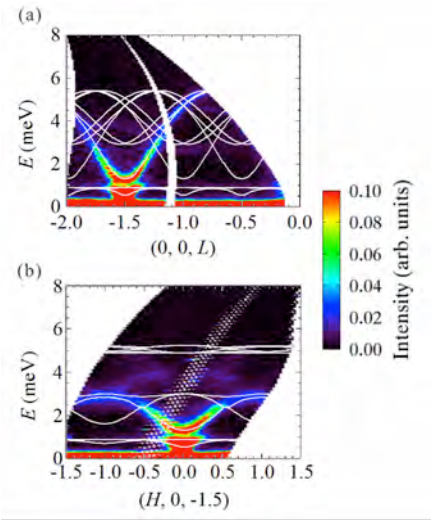

Fig. 21 Inelastic neutron scattering spectrum of $NdFe_3(BO_3)_4$ in case of (0,0,*L*) and (*H*,0,-1.5).

6.5 Multiferroic compounds

$RFe_3(BO_3)_4$ (*R*=rare earth metal) are a series of multiferroic compounds that crystallize trigonal structure with three fold screw chains of FeO_6 octahedra and R^{3+} ions along the crystallographic *c* direction. In *R* = Nd compound easy-plane type Néel order and spontaneous electric polarization appear simultaneously at $T_N = 30$ K. Weiss temperature is -115 K and the frustration ratio is -3.8. Thus the compound exhibits multiferroic property as well as the behavior of frustrated magnet. While magnetic structure was studied in detail [25], magnetic excitation was measured only by using electro-magnetic wave including ESR and Raman scattering techniques. INS experiment to measure the $S(\mathbf{q},w)$ in wide $\mathbf{q}$ space is the most effective method to identify the spin Hamiltonian realized in the compound. 22 pieces of single crystals are coaligned by X-ray Laue camera so that *a**-*c** plane is the scattering plane. Total mass of the sample for INS experiment is 2.1g. T0 chopper is set at 50Hz, 1.5° of collimator is installed in front of sample, and Fermi chopper, "S", with 200Hz is used to obtain high neutron flux. GM-type refrigerator was used to achieve 15 K. The sample was rotated to obtain the 3-dimensional $S(\mathbf{q},w)$. Figure 21 (a) and (b) show the spectrum cut along (0,0,*L*) and (*H*,0,-1.5) directions, respectively. Flat mode at $E \sim 1$meV is crystal field excitation of Nd ion, which was consistently observed by ESR and Raman scattering experiment [26,27]. The dispersive modes from collective excitations from Fe spins are observed at 2.5 meV < *E* < 5.5 meV. The obtained spectrum was analyzed by the minimal model of Heisenberg Hamiltonian including inchain interaction and interchain interaction between Fe spins, the interaction between Fe and Nd spins, single ion anisotropy of Fe spins, and effective mean field at Fe spins. The calculation, indicated by the white curves, reasonably reproduces the experimental result. We, thus, identified the effective Hamiltonian realized in $NdFe_3(BO_3)_4$. The detail will be discussed in the forthcoming publication.

6.6 Experimental confirmation of spin gap in antiferromagnetic alternating spin-3/2 chain substances $RCrGeO_5$ (R = Y or ^{154}Sm)

One interesting phenomenon in quantum spin systems is the appearance of a spin-singlet ground state

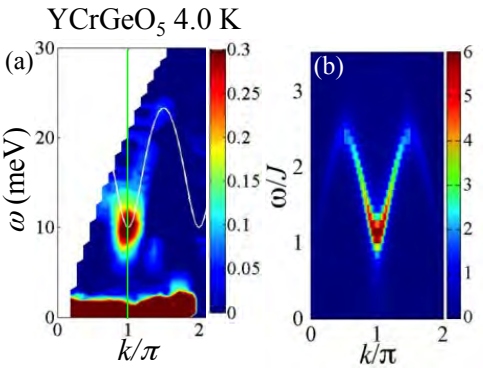

Fig. 22 Map of INS intensity in the *k*-ω plane of $YCrGeO_5$ at 4.0 K and $E_i = 51.1$ meV obtained using the conversion method. The horizontal axis indicates the normalized wavenumber parallel to the spin chain. The white line indicates $\omega(k) = \sqrt{21^2 \sin^2 k + 10^2}$. (b) The dynamical structure factor of the AF Heisenberg alternating spin-3/2 chain ($H = J\Sigma_i \left[1-(-1)^i \delta\right] \mathbf{S}_i \cdot \mathbf{S}_{i+1}$ with δ = 0.75) calculated using the dynamical density-matrix renormalization group method.

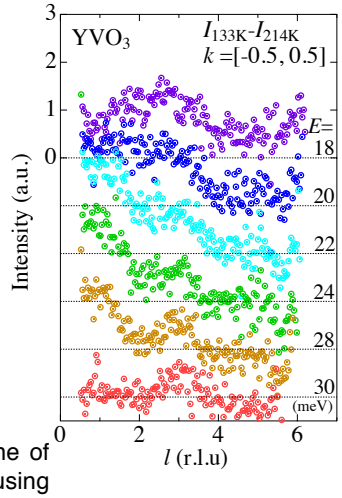

Fig. 23 INS spectra in the orbital ordered phase (133K), subtracted from that in the orbital disordered phase (214K). The horizontal axis *l* is the propagating direction of the predicted orbital waves.

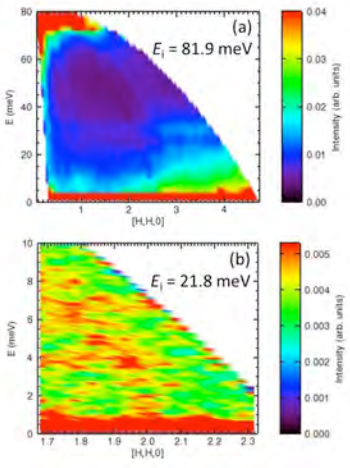

Fig. 24 Contour maps of intensity in $Cs_2Cu_3SnF_{12}$ as a function of energy and inplane wave vector for (a) $E_i = 81.9$ and (b) 21.8 meV. The intensity is integrated over the whole reachable range of (0,0,L) and (-K,K,0).

with a spin gap (singlet-triplet excitation). When the spin value is larger than 1, existence of a spin-singlet ground state with a spin gap has not been proved experimentally. We can expect anti- ferromagnetic (AF) alternating spin-3/2 chains of Cr^{3+} in $RCrGeO_5$ (R = Y or ^{154}Sm) and a spin-singlet ground state with a spin gap. We performed INS experiments on $RCrGeO_5$ (R = Y or ^{154}Sm) powders to confirm the spin gap excitations [28]. Excitations are apparent between 8 and 23 meV at 4.0 K in $YCrGeO_5$. Intensities of the excitations are strong in the small Q range and decrease with increasing T. Therefore, most of excitations are magnetic excitations. We could confirm a spin gap in the magnetic excitations. Qualitatively the same behaviors are observed in $^{154}SmCrGeO_5$. $RCrGeO_5$ (R = Y or ^{154}Sm) are the first spin-3/2 chain substances having a spin gap. Figure 22 (a) shows the map of neutron scattering intensity in the k-ω plane at 4.0 K obtained using the conversion method developed by Tomiyasu et al. The results correspond to results of a single crystal measured along the spin chain direction. The intensity is the strongest around $k = \pi$ as expected in AF spin chains. The magnetic excitations have a dispersion relation. The white line shows the empirical dispersion relation of the lowest magnetic excitations and the spin gap is estimated as 10 meV. Figure 22 (b) shows the calculated dynamical structure factors of the AF Heisenberg alternating spin-3/2 chains. The experimental result agrees well with the calculation.

6.7 Search of orbital waves in YVO_3

The orthorhombic perovskite YVO_3 shows the G-type orbital ordering in the T range from 77 to 200 K [29]. In this phase, the existence of large orbital fluctuations is suggested [30], and dispersive orbital waves propagating along the c-axis, due to the 1D spin-orbital correlations, is predicted [31]. In consideration of the neutron scattering cross-section obtained from the correlation function for the orbital angular moment, we have attempted to detect the orbital waves. Figure 23 shows observed spectra in the orbital ordered phase (133 K), subtracted from those in the orbital disordered phase (214 K). The intensity decreases with increasing $|\boldsymbol{Q}|$, where $\boldsymbol{Q} = h\boldsymbol{a}^*+k\boldsymbol{b}^*+l\boldsymbol{c}^*$, which can be explained by the magnetic form factor for the V^{3+} orbital. In addition, we found the intensity shows a periodic behavior with the maximum at l = odd number. This indicates that the observed spectra might be originated from the orbital waves. This experiment was performed using the fine-resolution Fermi-chopper spectrometer, SEQUOIA at SNS, ORNL, as one of the substituted proposals for the disaster of the earthquake on 11 March 2011.

6.8 Kagome lattice antiferromagnet

Geometrical frustrated systems with reduced spatial dimensionality have gathered considerable interest. They can suppress conventional magnetic orders, and eventually induce novel states of magnetism. Here we concentrate on Kagome lattice antiferromagnet (KAF), which composes of corner-sharing triangles. Since no candidate material of KAF with exact lattice geometry and strong two-dimensionality have so far been reported, low-T magnetism remains to be controversial. There have indeed reported several scenarios to describe magnetism of KAF in theories. One of intriguing subjects is if the excitation from nonmagnetic ground state to magnetic excited state is gapfull or gapless. We have recently examined a prominent example of S = 1/2 systems, $Rb_2Cu_3SnF_{12}$, and revealed the pinwheel valence bond solid ground state. In addition, an analogue $Cs_2Cu_3SnF_{12}$with S = 1/2 is revealed to magnetically order into so-called Q = 0 structure. Through INS experiments, we successfully estimated coupling constants of spins. To gain further insight into detailed view of magnetic excitations of this compound, we performed an INS measurement on the HRC. A single crystal is mounted on the (HHL) horizontal scattering plane and the (00L) was set to be parallel to the incident neutron beam. We measured spectra at T = 5 K using a CCR with E_i = 81.9 meV. Due to lack of sample mass and beam intensity, we were unable to obtain conclusive data and only phonon signals were observed at high-Q regime (Fig. 24 (a)). Owing to the multi-E_i system of the HRC, however, we succeeded in detecting magnetic signals spanning G-point (2,2,0) to K-point (5/3,5/3,0) with E_i = 21.8 meV, which is good accord with recent results of triple-axis and AMATERAS spectrometers (Fig. 24 (b)). We will hereafter pursue its magnetic origin, and induce quantum critical phenomena by diluting such chemically analogous systems showing distinct low-T magnetism.

7. Toward eV Neutron Spectroscopy

7.1 Spin density waves in chromium

The spin-density wave (SDW) in Cr is one of the most fascinating subjects in condensed matter physics. It has a history of long and continuing research. One of the open issues is its magnetic excitation, which arises from incommensurate magnetic Bragg positions with a steep dispersion slope and extends to more than 600 meV. In

order to examine the detailed structure of high-energy magnetic excitations of Cr in ($\boldsymbol{Q}$,ω) space, we performed magnetic INS on the HRC using a single crystal with 4 cc in volume. Figure 25 shows an intensity contour map in the longitudinally-spin- polarized SDW state, where the intensity is projected on (2, *k*, *l*) plane over a wide energy range. Sharp spots appears at three magnetic Γ points: (2, -1, 0) at ω = 250 meV, and (2, 0, ±1) at ω = 150 meV. The line-cutting profiles along *l* direction evince that the magnetic cross sections are well localized in $\boldsymbol{Q}$ space. No consensus has been established yet for this novel high-energy excitation. One scenario is based on spin-wave excitations from a pseudo localized-spin system with a zone boundary energy of ~1 eV, though Cr is usually regarded as a typical itinerant-electron system. Another possibility comes from electron excitations across the Fermi energy, possibly reflecting the peculiar Fermi surfaces. Further experimental studies toward high-energy region are required not only to settle such the argument, but also to get a clue to unknown spin dynamics in metallic magnets.

7.2 Intermultiplet transition in filled skutterudite compound $SmFe_4P_{12}$

Samarium-based filled skutterudite $SmFe_4P_{12}$ was reported to be the first ferromagnetic Kondo- lattice compound. It shows an unconventional heavy-electron state with the large electronic specific-heat coefficient 370 mJ/mol K^2 and a ferromagnetic transition at 1.6 K. Although the 4f electrons clearly have a key role in a formation of heavy quasiparticle at low *T*, there has been lack of basic information about the 4*f* electronic states in this system because neutron scattering experiments on materials containing thermal neutron absorber elements such as Sm. To avoid this problem, thus we have done INS experiment on $SmFe_4P_{12}$ by using higher energy neutrons. Figure 26 shows the INS spectra of polycrystalline $SmFe_4P_{12}$ at 6.5 K and 280 K. The sample was prepared by using a tin flux method, where natural abundant Sm isotopes were used. In low *Q* range, a small peak around 80 ~ 90 meV is observed at low *T*. This peak is not visible in high *Q* range, indicating that it is of magnetic origin. If this peak is associated with the intermultiplet transition from *J* = 5/2 ground state to *J* = 7/2 multiplet, interestingly, the energy splitting is very small compared to usual Sm-based compounds. This might originate from the strong *c-f* hybridization in filled skutterudite compounds.

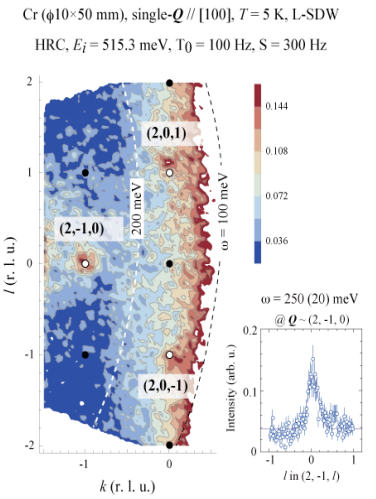

Fig. 25 Intensity contour onto (2, *k*, *l*) plane with a thickness of 1.9 ≤ *h* ≤ 2.1. The inset shows a line cut profile along l at (2, -1, 0) integrating within a range of 1.9 ≤ *h* ≤ 2.1 and -1.1 ≤ *k* ≤ -0.9.

7.3 Possibility of observation of electronic excitations

The neutron might become a probe observing electronic excitations. It has been predicted novel magnetic excitations in the halogen bridged nickel complex, $[Ni(chxn)_2Br]Br_2$, which is a 1D charge transfer insulator. Recently, the 1D extended Hubbard model has been developed for describing the physical properties in this system. The optical conductivity spectrum suggests an interaction of spins to charge excitations. Also, by an angle-resolved photoemission spectroscopy, a clear spin-charge separation has not been observed in this system, whereas it has been clearly observed in the 1D cuprates such as $SrCuO_2$ and Sr_2CuO_3. Such behaviors in this nickel complex might be attributed to a coupling between spin and charge, because the charge excitation energies are reduced to be comparable to the magnetic excitation energies resulting from reduction of the on-site Coulomb repulsion via perturbation of the inter-site Coulomb repulsion. As the result, magnons at low energy region as well as spin-induced charge excitations at high energy region are predicted [32]. The detection of spin-induced charge excitations will be a direct experiment adding a new knowledge in physics on the freedoms of spin and charge. However, this experiment has not yet been started, because a sizable fully-deuterated single crystal required for INS experiments has not yet been synthesized. We are now trying another example.

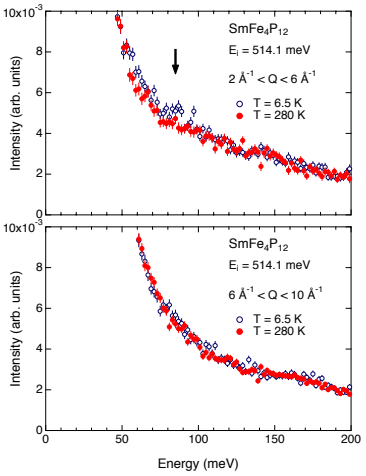

Fig. 26 INS spectra of $SmFe_4P_{12}$ at *T* = 6.5 K and 280 K for (a) momentum transfer range of 2 $Å^{-1}$ < *Q* < 6 $Å^{-1}$ and (b) 6 $Å^{-1}$< *Q* < 10 $Å^{-1}$.

8. Summary

We constructed the HRC, since then, we have continuously improved this spectrometer at many points. We could achieve the best performance of the

HRC in the current technology. It should be noted that the NBS experiments have been feasible on the HRC by reducing background at low angles as well as increasing the neutron flux, and some results have been obtained by this technique. In the high resolution experiments in the conventional energy momentum space, many studies on spin dynamics in materials with current interest in correlated electron systems are in progress. We have started sub-eV neutron spectroscopy to detect high energy magnetic excitations, and also, we are planning to observe electronic excitations.

References

[1]* S. Itoh, T. Yokoo, S. Satoh, S. Yano, D. Kawana, J. Suzuki and T. J. Sato, Nucl. Instr. Meth. Phys. Res. A 631 (2011) 90.
[2]* S. Yano, S. Itoh, S. Satoh, T. Yokoo, D. Kawana, and T. J. Sato, Nucl. Instr. Meth. Phys. Res. A 654 (2011) 421.
[3]* S. Itoh, K. Ueno, R. Ohkubo, H. Sagehashi, Y. Funahashi and T. Yokoo, Nucl. Instr. Meth. Phys. Res. A 661 (2012) 86.
[4]* S. Itoh, K. Ueno, R. Ohkubo, H. Sagehashi, Y. Funahashi and T. Yokoo, Nucl. Instr. Meth. Phys. Res. A 654 (2011) 527.
[5]* S. Itoh, K. Ueno and T. Yokoo, Nucl. Instr. Meth. Phys. Res. A 661 (2012) 58.
[6]* S. Itoh, T. Yokoo, T. Yokoo, J. Suzuki, T. Teraoku and M. Tsuchiya, Nucl. Instr. Meth. Phys. Res. A 670 (2012) 1.
[7]* T. Yokoo, N. Kaneko, S. Itoh, T. Otomo, K. Suzuya, Y. Suetsugu, M. Shirai, Rev. Sci. Instrum. 82 (2011) 095109.
[8]* S. Itoh, T. Yokoo, D. Kawana, H. Yoshizawa, T. Masuda, M. Soda, T. J. Sato, S. Satoh, M. Sakaguchi and S. Muto, J. Phys. Soc. Jpn. 82 (2013) SA033.
[9]* S. Itoh, T. Yokoo, D. Kawana and Y. Endoh, J. Phys. Soc. Jpn. 82 (2013) SA034.
[10]* S. Itoh, Y. Endoh, T. Yokoo, D. Kawana, Y. Kaneko, Y. Tokura and M. Fujita, J. Phys. Soc. Jpn. 82 (2013) 043001.
[11]* S. Itoh, T. Yokoo, D. Kawana, Y. Kaneko, Y. Tokura, M. Fujita, K. Yoshida, K. Saito, N. Inami, Y. Takeichi, K. Ono, Y. Endoh, J. Phys.: Conf. Series 502 (2014) 012043.
[12]* S. Itoh, Y. Endoh, T. Yokoo, J.-G. Park, Y. Kaneko, Y. Tokura, N. Nagaosa, unpublished (2014).
[13] H. M. Mayer et al., J. Magn. Magn. Mater. 97 (1991) 210.
[14]* K. Ono, N. Inami, K. Saito, Y. Takeichi, M. Yano, T. Shoji, A. Manabe, A. Kato, Y. Kaneko, D. Kawana, T. Yokoo , and S. Itoh, J. Appl. Phys. 115 (2014) 17A714.
[15] J. Teixeira et al., Phys. Rev. Lett. 54 (1985) 2681.
[16] G. Ruocco et al., Nature 379 (1996) 521.
[17] A. Orecchini et al., J. Am. Chem. Soc. 131 (2009) 4664.
[18]* S. Itoh, T. Yokoo, S. Yano, D. Kawana, H. Tanaka and Y. Endoh, J. Phys. Soc. Jpn. 81 (2012) 084706.
[19] K. Tajima, Y. Ishikawa, and H. Obara, J. Magn. Magn. Mater. 15-18 (1980) 373.
[20] Y. Todate, K. Yamada, Y. Endoh, and Y. Ishikawa, J. Phys. Soc. Jpn. 56 (1987) 36.
[21]* S. Yano, S. Itoh, T. Yokoo, S. Satoh, D. Kawana, Y. Kousaka, J. Akimitsu and Y. Endoh, J. Magn. Magn. Mater. 347 (2013) 33.
[22]* S. Itoh, S. Yano, T. Yokoo, S. Satoh, D. Kawana, Y. Kousaka, J. Akimitsu, Y. Endoh, J. Phys.: Conf. Series 502 (2014) 012044.
[23] T. Yamazaki et al., J. Phys. Soc. Jpn. 83 (2014) 054711.
[24]* T. Yokoo, S. Itoh, S. Ibuka, H. Yoshizawa, J. Akimitsu, J. Phys.: Conf. Series 502 (2014) 012045.
[25] M. Janoscheket et al., Phys. Rev. B 81 (2010) 094429.
[26] A. M. Kuz'menko et al., JETP Lett. 94 (2011) 294.
[27] M. N. Popova, Phys. Rev. B 75 (2007) 224435.
[28]* M. Hase, M. Soda, T. Masuda, D. Kawana, T. Yokoo, S. Itoh, A. Matsuo, K. Kindo, and M. Kohno, Phys. Rev. B 90 (2014) 024416.
[29] S. Miyasaka et al., Phys. Rev. B 73 (2006) 224436.
[30] C. Ulrich et al., Phys. Rev. Lett. 91 (2003) 257202.
[31] S. Ishihara, Phys. Rev. B 69 (2004) 075118.
[32] N. Tomita and K. Nasu, Phys. Rev. B 61 (2000) 2488.

* results from this project.